Sterile neutrino portal dark matter with Z_3 symmetry

An Liu,[1] Zhi-Long Han,[1,*] Yi Jin,[1,2] and Honglei Li[1]

[1]*School of Physics and Technology, University of Jinan, Jinan, Shandong 250022, China*
[2]*Guangxi Key Laboratory of Nuclear Physics and Nuclear Technology, Guangxi Normal University, Guilin, Guangxi 541004, China*

(Received 27 June 2023; accepted 26 September 2023; published 26 October 2023)

In this paper, we consider the sterile neutrino portal dark matter with Z_3 symmetry. This model further extends the canonical type-I seesaw with a fermion singlet χ and a scalar singlet ϕ. Under the Z_3 symmetry, the dark sector transforms as $\chi \to e^{i2\pi/3}\chi$, $\phi \to e^{i2\pi/3}\phi$, while the standard model particles and the sterile neutrino N transform trivially. In addition to the interactions as $y_N\phi\bar{\chi}N$ and $\lambda_{H\phi}(H^\dagger H)(\phi^\dagger\phi)$ allowed in the Z_2 symmetry, the Z_3 symmetry also introduces two new terms, i.e., $y_\chi\phi\overline{\chi^c}\chi$ and $\mu\phi^3/2$. These new interactions induce additional semiannihilation processes as $\chi\chi \to N\chi$ and $\phi\phi \to h\phi$ for the weakly interacting massive particle dark matter. We then perform a comprehensive analysis of the phenomenology of this Z_3 symmetric model. Viable parameter space is explored under the constraints from dark matter relic density, Higgs invisible decay, and indirect and direct detection for both fermion and scalar dark matter. We find that the semiannihilation channels $\chi\chi \to N\chi$ and $\phi\phi \to N\chi$ can lead to quite different phenomena from the Z_2 symmetric model, which provides a viable pathway to distinguish these two kinds of model.

DOI: 10.1103/PhysRevD.108.075021

I. INTRODUCTION

The identity of particle dark matter (DM) and the explanation for the tiny mass of neutrinos remain outstanding questions in particle physics, garnering attention as crucial topics in current research. Their common origin presents the possibility of future exploration into new physics beyond the standard model. The weakly interacting massive particle (WIMP) is one of the most promising dark matter candidates [1]. However, this scenario, such as the extensively studied Higgs portal [2–4] and Z' portal model [5–8], usually suffers stringent constraints from direct detection. Therefore, a new interaction portal for the WIMP dark sector should be considered.

Sterile neutrinos N are introduced to generate the tiny neutrino mass via the canonical type-I seesaw mechanism [9,10]. For a proper mixing angle with active neutrinos, the keV scale sterile neutrino can serve as a decaying dark matter [11,12]. Then the radiative decay $N \to \nu\gamma$ leads to an observable signature at x-ray telescopes [13], which is able to explain the tentative 3.5 keV line signal [14]. However, the parameter space for sterile neutrino dark matter now is tightly constrained [15]. If the sterile neutrinos N are charged under the dark group, the lightest sterile neutrino becomes a stable dark matter. In this scenario, the tree-level type-I seesaw is also forbidden by the dark group, then light neutrino mass could be generated via the radiative mechanism [16–19].

On the other hand, the electroweak scale sterile neutrino N is an ideal messenger between the dark sector and the standard model [20–30]. This is facilitated through the new Yukawa coupling $y_N\phi\bar{\chi}N$, which enables the secluded channel $\phi\phi/\chi\chi \to NN$, providing an additional annihilation pathway for the WIMP dark matter. In particular, this scenario features a relatively small nucleon scattering cross section and permits the indirect detection of observable gamma-ray signals [31–36]. For an electroweak scale, dark matter annihilating via the sterile neutrino portal, which is still allowed by direct detection, will hopefully be probed by indirect detection in the near future. Meanwhile, the sterile neutrino portal dark matter produced through the freeze-in mechanism is also extensively studied [37–44].

The interactions between the dark sector and the standard model particles are typically governed by the dark group, such as the well-studied Z_2 [45] or $U(1)_{B-L}$ symmetry [46]. Although the simplest Z_2 symmetry has demonstrated success in dark matter with a simplified phenomenology, more sophisticated dark groups, e.g., $Z_N(N \geq 3)$ [47], A_4 [48], and $SU(2)$ symmetry [49], are also options. For instance, an alternative explanation for the observed relic abundance of dark matter via semiannihilation may be

*sps_hanzl@ujn.edu.cn

achieved by introducing the next simplest Z_3 symmetry, which leads to a lower bound on the direct detection cross section [50–52].

In this paper, we consider the sterile neutrino portal dark matter with Z_3 symmetry [53,54]. This model includes a fermion singlet χ and a scalar singlet ϕ, both of which transform nontrivially under the exact Z_3 symmetry as $\chi \to e^{i2\pi/3}\chi$, $\phi \to e^{i2\pi/3}\phi$. The standard model particles and the sterile neutrinos are not charged under the imposed Z_3 symmetry. Compared with the Z_2 symmetry, the Z_3 symmetry allows two new interaction terms, i.e., $y_\chi \phi \overline{\chi^c}\chi$ and $\mu\phi^3/2$, which would lead to new annihilation channels of dark matter. The semiannihilation of fermion dark matter via the process $\chi\chi \to N\chi$ in the framework of effective field theory has been considered in Ref. [53]. Focusing on the self-interaction of dark scalar ϕ, Ref. [54] studies the nonthermal production of dark matter χ by the late time decay $\phi \to \chi\nu$. In this paper, we perform a comprehensive analysis of WIMP dark matter for both scalar and fermion scenarios. Nonthermal production of dark matter will be considered in a separate paper [55].

This paper is structured into several sections. In Sec. II, we introduce the sterile neutrino portal dark matter model with Z_3 symmetry. In Sec. III, we illustrate the evolution of the dark matter abundance under certain scenarios. We then perform a random scan to obtain the viable parameter space for the correct relic abundance. In Sec. IV, we calculate the branching ratio of Higgs invisible decay. In Sec. V, we explore the indirect detection constraints on dark matter. In Sec. VI, we calculate the direct detection cross section of dark matter. Finally, in Sec. VII, we provide concluding remarks on our study.

II. THE MODEL

This model further extends the type-I seesaw with a dark sector under Z_3 symmetry. Sterile neutrinos N are introduced to generate tiny neutrino mass. In this paper, we consider the electroweak scale N in order to accommodate WIMP dark matter. The dark sector consists of a scalar singlet ϕ and a fermion singlet χ. Under the dark Z_3 symmetry, the dark sector transforms as $\chi \to e^{i2\pi/3}\chi$, $\phi \to e^{i2\pi/3}\phi$, while the standard model particles and the sterile neutrinos transform trivially. The lightest particle in the dark sector serves as dark matter. In this paper, both fermion and scalar dark matter will be considered.

The Yukawa interaction takes the form of

$$-\mathcal{L}_Y = \left(y_\nu \overline{L}\tilde{H}N + y_N \phi \bar{\chi} N + \text{H.c.}\right) + y_\chi \phi \overline{\chi^c}\chi, \quad (1)$$

where L is the left-handed lepton doublet and H is the Higgs doublet with $\tilde{H} = i\sigma_2 H^*$. Light neutrino mass is generated by the type-I seesaw as

$$m_\nu = -\frac{v^2}{2} y_\nu m_N^{-1} y_\nu^T, \quad (2)$$

where $v = 246$ GeV is the vacuum expectation value of the Higgs field. For electroweak scale sterile neutrinos, the mixing angle with light neutrino θ is at the order of $\sqrt{m_\nu/m_N} \sim 10^{-6}$, which is far below current collider limits [56].

The scalar potential under the exact Z_3 symmetry is

$$V = -\mu_H^2 H^\dagger H + \mu_\phi^2 \phi^\dagger\phi + \lambda_H (H^\dagger H)^2 + \lambda_\phi (\phi^\dagger\phi)^2 + \lambda_{H\phi}(H^\dagger H)(\phi^\dagger\phi) + \left(\frac{\mu}{2}\phi^3 + \text{H.c.}\right), \quad (3)$$

where all the parameters are taken to be real. After the electroweak symmetry breaking, the physical mass of the dark scalar ϕ is $m_\phi^2 = \mu_\phi^2 + \lambda_{H\phi} v^2/2$. The scalar potential in Eq. (3) must have a finite minimum to prevent unbounded energy, which requires [51]

$$\lambda_H > 0, \qquad \lambda_\phi > 0, \qquad \lambda_{H\phi} + 2\sqrt{\lambda_H \lambda_\phi} > 0. \quad (4)$$

Meanwhile, the stability of the electroweak vacuum sets an upper bound on the cubic coupling μ as

$$\mu \le 2\sqrt{\lambda_\phi} m_\phi, \quad (5)$$

in the limit of small $\lambda_{H\phi}$. In order to maintain the validity of perturbation theory, $|\lambda_\phi| \le \pi$ and $|\lambda_{H\phi}| \le 4\pi$ should be further satisfied. In the following studies, we assume $\mu < 3m_\phi$, which is also allowed by the unitarity constraints [57].

III. RELIC DENSITY

In this section, we first discuss the annihilation channels of dark matter. As shown in Fig. 1, there are two dominant annihilation channels for the fermion dark matter χ. One is the secluded channel $\chi\chi \to NN$, which also exists in the Z_2 symmetry model. The other one is the semiannihilation channel $\chi\chi \to N\chi$ [58], which is induced by the new Yukawa coupling $y_\chi \phi \overline{\chi^c}\chi$ under the Z_3 symmetry. In principle, there is also the scalar semiannihilation channel $\chi\chi \to \phi h$; however, the annihilation cross section is p-wave suppressed for the Majorana-like Yukawa coupling $y_\chi \phi \overline{\chi^c}\chi$ [59,60]. For the scalar dark matter ϕ, there are four kinds of annihilation channels as depicted in Fig. 2. Apart from the extensively studied Higgs portal channels $\phi\phi \to$ SM, the secluded channel $\phi\phi \to NN$ is also allowed. Meanwhile, the cubic term $\mu\phi^3$ and the Yukawa coupling $y_\chi \phi \overline{\chi^c}\chi$ induce

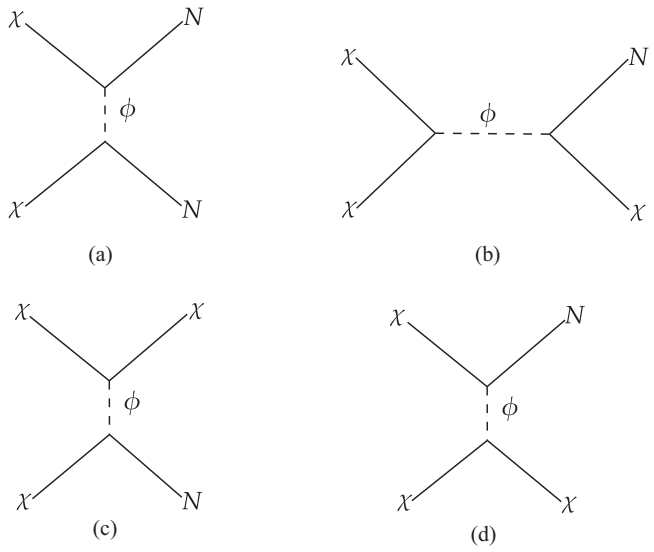

FIG. 1. The dominant annihilation channels of fermion dark matter. (a) The secluded channel $\chi\chi \to NN$. (b)–(d) The semiannihilation channel $\chi\chi \to N\chi$.

two additional semiannihilation channels $\phi\phi \to N\chi$ and $\phi\phi \to h\phi$ if kinematically allowed. Compared with the simplest Z_3 scalar singlet dark matter [57], the fermion channel $\phi\phi \to N\chi$ is unique in this model. Therefore, the sterile neutrino portal semiannihilation channels $\chi\chi \to N\chi$ and $\phi\phi \to N\chi$ provide a viable pathway to distinguish from the other models. It is notable that when masses of the dark sector are nearly degenerate, the coannihilation channels such as $\phi\chi \to h\chi/\phi N$ are also possible. For simplicity, we do not consider such coannihilation channels in this paper.

As the WIMP dark matter candidate, it is initially in thermal equilibrium and then decouples from the thermal bath at sufficiently low temperature. Defining the variable $z = m_{\rm DM}/T$, evolution of the fermion dark matter abundance Y_χ is determined by the Boltzmann equation

$$\frac{dY_\chi}{dz} = -\frac{\lambda}{z^2}\langle\sigma v\rangle_{\chi\chi\to NN}\left(Y_\chi^2 - (Y_\chi^{\rm eq})^2\right) - \frac{\lambda}{2z^2}\langle\sigma v\rangle_{\chi\chi\to N\chi}\left(Y_\chi^2 - Y_\chi^{\rm eq}Y_\chi\right), \tag{6}$$

where λ is defined as $\lambda \equiv \sqrt{\pi g_*/45}\, m_{\rm DM} M_{\rm Pl}$. Here, g_* is the effective number of degrees of freedom of the relativistic species and $M_{\rm Pl} = 1.2 \times 10^{19}$ GeV is the Planck mass. The sterile neutrino N is assumed in thermal equilibrium [61]. Similarly, evolution of the scalar dark matter is calculated as

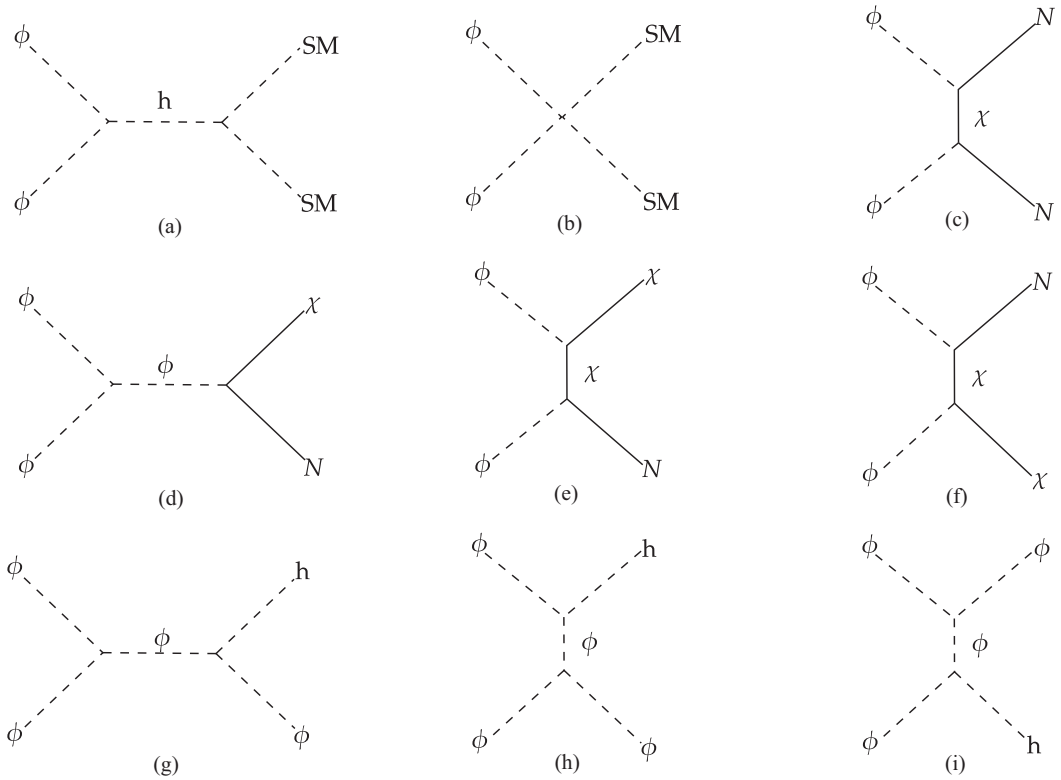

FIG. 2. The dominant annihilation channels of scalar dark matter. (a),(b) The annihilation channels to standard model (SM) final states. (c) The secluded channel $\phi\phi \to NN$. (d)–(f) The fermion semiannihilation channel $\phi\phi \to N\chi$. (g)–(i) The scalar semiannihilation channel $\phi\phi \to h\phi$.

$$\frac{dY_\phi}{dz} = -\frac{\lambda}{z^2}\langle\sigma v\rangle_{\phi\phi\to \mathrm{SM}}\left(Y_\phi^2 - (Y_\phi^{\mathrm{eq}})^2\right) - \frac{\lambda}{2z^2}\langle\sigma v\rangle_{\phi\phi\to h\phi}\left(Y_\phi^2 - Y_\phi^{\mathrm{eq}} Y_\phi\right)$$
$$-\frac{\lambda}{z^2}\langle\sigma v\rangle_{\phi\phi\to NN}\left(Y_\phi^2 - (Y_\phi^{\mathrm{eq}})^2\right) - \frac{\lambda}{2z^2}\langle\sigma v\rangle_{\phi\phi\to N\chi}\left(Y_\phi^2 - \frac{(Y_\phi^{\mathrm{eq}})^2}{Y_\chi^{\mathrm{eq}}} Y_\chi\right). \quad (7)$$

The thermally averaged cross sections $\langle\sigma v\rangle$ are calculated with MicrOMEGAs [62].

The above calculations assume kinetic equilibrium between the dark sector and the SM. However, with the suppressed scattering cross section of the dark sector and SM, e.g., for $y_\nu \sim 10^{-8}$ and $\lambda_{H\phi} \sim 10^{-6}$, kinetic decoupling of the dark sector from the SM would happen before the dark matter chemical freeze-out [29]. For fermion dark matter, kinetic equilibrium is maintained through the elastic scattering process $\chi N \to \chi N$. When the sterile neutrino N is relativistic at the time of dark matter freeze-out, e.g., $m_N < m_\chi/20$, the temperature of the dark sector is similar to that of the SM bath. The study in Ref. [29] shows that a 20% correction to the relic abundance is possible. Meanwhile, if the sterile neutrino becomes nonrelativistic at dark matter freeze-out, an order one correction to the relic abundance is expected [63]. For scalar dark matter, the early kinetic decoupling effects are significant at the Higgs resonance region [63]. Correction to the relic abundance is mild for the semiannihilation channel, although the kinetic equilibrium is not realized at the time of chemical freeze-out [57].

Figures 3 and 4 present the evolution of the dark matter relic abundance via various annihilation channels during the early Universe. According to the general definition, the lighter of fermion χ and scalar ϕ is the dark matter candidate. For illustration, we set the dark matter mass $m_{\mathrm{DM}} = 500$ GeV, the other heavier particle mass $m_{\mathrm{Heavier}} = 800$ GeV, and the sterile neutrino mass $m_N = 180$ GeV. The secluded channel $\chi\chi \to NN$ only involves the Yukawa coupling y_N, whose impacts on the abundance is shown in Fig. 3(a). The contribution of the semiannihilation channel $\chi\chi \to N\chi$ is turned off simply by setting $y_\chi = 0$. To obtain correct relic abundance, $y_\chi \sim \mathcal{O}(0.1)$ is required when $\chi\chi \to NN$ is the only annihilation channel. For the process $\chi\chi \to N\chi$, both the Yukawa coupling y_N and y_χ contribute. We then fix $y_N = 0.2$ and show the impact of y_χ in Fig. 3(b). The observed relic abundance is reproduced with $y_\chi \sim \mathcal{O}(1)$. Since $\chi\chi \to NN$ is also kinematically allowed, it is clear that, when $y_\chi \ll y_N$, the relic abundance is actually determined by the secluded channel.

For the scalar dark matter ϕ, we first show the impact of $\lambda_{H\phi}$ on the canonical Higgs portal annihilation channels in Fig. 4(a). Contributions of other kinds of annihilation channels are forbidden by fixing $y_\chi = y_N = 0$ and $\mu = 0$ GeV. These Higgs portal channels are efficient to obtain the desired abundance with $\lambda_{H\phi} \gtrsim \mathcal{O}(0.01)$. The contribution of scalar semiannihilation $\phi\phi \to h\phi$ is depicted in Fig. 4(b), while setting $\lambda_{H\phi} = 0.05$. A relatively large cubic coupling $\mu \gtrsim 100$ GeV is required to make this channel the dominant one. In Figs. 4(c)–4(f), we consider the secluded channel $\phi\phi \to NN$ and fermion semiannihilation channel $\phi\phi \to N\chi$. Similar to the fermion dark matter scenario, correct abundance is achieved with $y_N \sim \mathcal{O}(0.1)$ or $y_\chi \sim \mathcal{O}(1)$ when $\phi\phi \to NN$ or $\phi\phi \to N\chi$ is the dominant annihilation channel, respectively. Different from

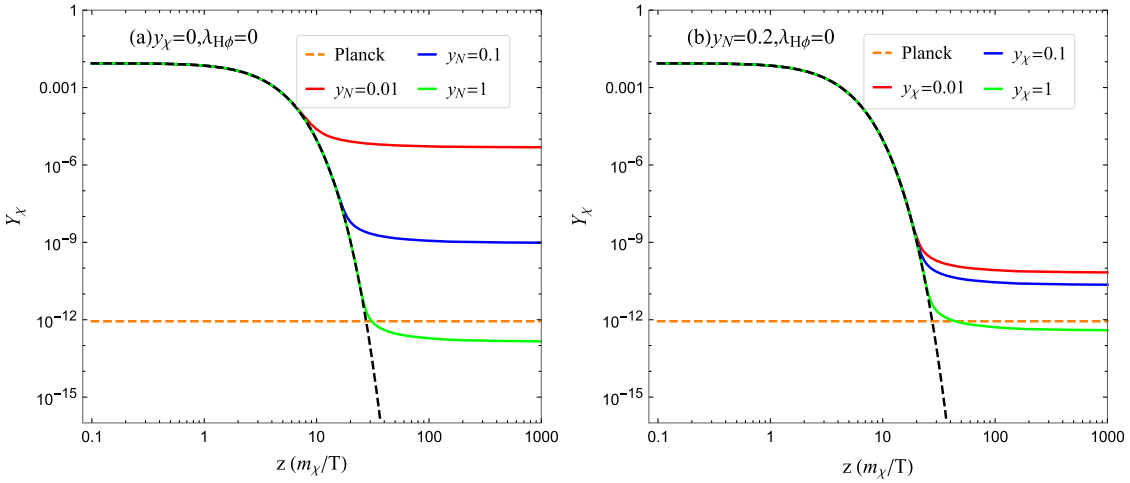

FIG. 3. The evolution of fermion dark matter abundance in different major annihilation channels. The orange horizontal lines correspond to the Planck observed abundance for $m_{\mathrm{DM}} = 500$ GeV. The evolution of the fermion dark matter abundance via (a) the secluded annihilation channel $\chi\chi \to NN$, and (b) the semiannihilation channel $\chi\chi \to N\chi$.

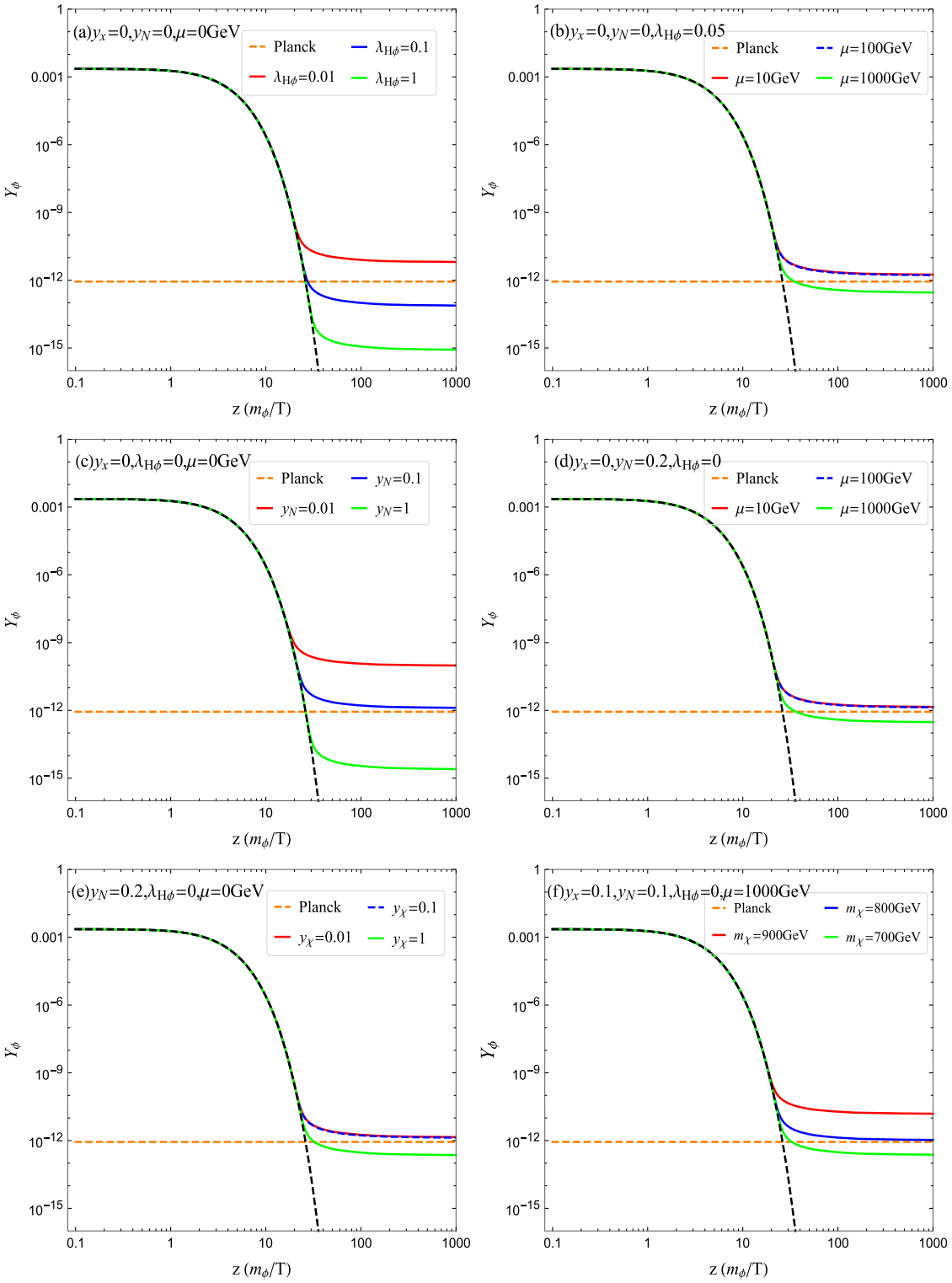

FIG. 4. Same as Fig. 3, but for scalar dark matter. The evolution of the scalar dark matter abundance via (a) Higgs portal annihilation channels $\phi\phi \to$ SM, (b) scalar semiannihilation channel $\phi\phi \to h\phi$, (c) secluded annihilation channel $\phi\phi \to NN$, (d)–(f) fermion semiannihilation channel $\phi\phi \to N\chi$.

the fermion dark matter, the s channel of semiannihilation $\phi\phi \to N\chi$ is induced by the cubic term $\mu\phi^3$, but not the Yukawa coupling $y_\chi \phi \overline{\chi^c}\chi$. The contributions of the s and t/u channels are then separately shown in Figs. 4(d) and 4(e). Since the contribution of $\phi\phi \to N\chi$ is suppressed by the final states' phase space in the benchmark points, a larger contribution is possible with lighter χ, N, which is illustrated in Fig. 4(f).

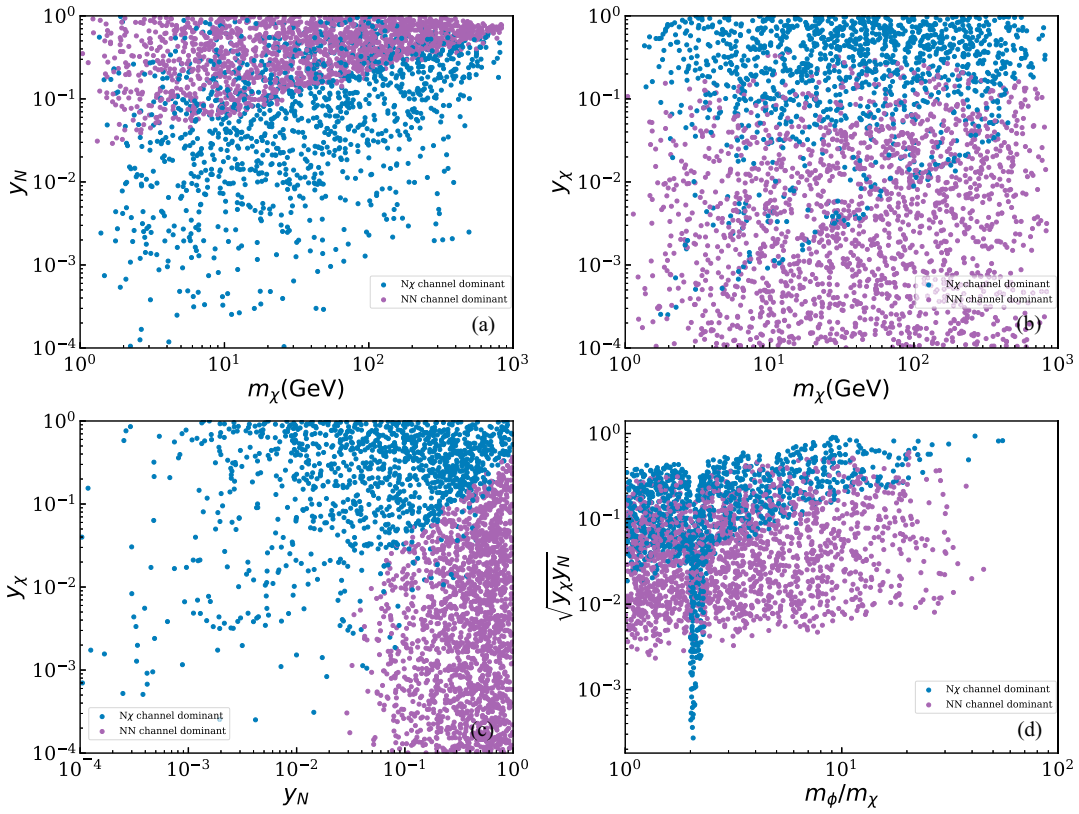

FIG. 5. Distributions of samples with correct relic density for fermion dark matter. The purple and blue points denote that the dominant annihilation channel is $\chi\chi \to NN$ and $\chi\chi \to N\chi$, respectively. Projection of allowed samples on (a) $y_N - m_\chi$ plane, (b) $y_\chi - m_\chi$ plane, (c) $y_N - y_\chi$ plane, and (d) $\sqrt{y_\chi y_N} - m_\phi/m_\chi$ plane.

Generating the appropriate cosmological relic density, as determined with high accuracy by the Planck experiment $\Omega_{\rm DM}h^2 = 0.120 \pm 0.001$ [64] is a crucial prerequisite for a viable dark matter candidate. With a seesaw related mixing angle $\theta \sim \sqrt{m_\nu/m_N}$, the lifetime of sterile neutrino τ_N would be longer than $\mathcal{O}(0.1)$ s for $m_N < 1$ GeV, which is excluded by big bang nucleosynthesis [65]. So we assume $m_N > 1$ GeV in this paper and then perform a random scan to explore the following dark sector parameter space:

$$y_{\chi,N} \in [10^{-4}, 1], \qquad \lambda_{H\phi} \in [10^{-6}, 1],$$
$$\mu/m_\phi \in [0, 3], \qquad m_{\chi,\phi} \in [1, 10^3]\ \text{GeV}. \tag{8}$$

Samples with correct relic density in the 3σ range of the Planck value are kept for later study. Survived samples are then classified by the dominant annihilation channels. The results are shown in Figs. 5 and 6 for the case of fermion and scalar dark matter, respectively. When $\chi\chi \to NN$ is the dominant channel, it is clear in Fig. 5(a) that a lower bound on y_N exists, which is approximately $y_N \gtrsim (m_\chi/10^4\ \text{GeV})^{1/2}$. Including the contribution of semiannihilation channel $\chi\chi \to N\chi$ would allow y_N to be about 2 orders of magnitude smaller. Similarly, the lower limit $y_\chi \gtrsim m_\chi/10^4$ GeV should be satisfied when $\chi\chi \to N\chi$ is the dominant channel. It is also clear in Fig. 5(b) that, for large enough y_χ, i.e., $y_\chi \gtrsim 0.3$, the semiannihilation channel will always be the biggest contribution. These two channels are well separated in the $y_N - y_\chi$ plane, namely, $\chi\chi \to N\chi$ is the leading one when $y_\chi \gtrsim 0.6 y_N$. As shown in Fig. 1(b), there is an s channel for the $\chi\chi \to N\chi$ annihilation. Therefore, the contribution of this channel is enhanced when $m_\phi \simeq 2m_\chi$, which leads to the deep cusp in Fig. 5(d). Apart from the resonance region, the larger the ratio m_ϕ/m_χ is, the bigger the factor $\sqrt{y_\chi y_N}$ is required.

For the scalar dark matter, $\lambda_{H\phi} \lesssim 0.1$ is enough to achieve the correct relic density when $10 \lesssim m_\phi \lesssim 10^3$ GeV as shown in Fig. 6(a). The sharp dip around $m_\phi \sim m_h/2$ corresponds to the on shell production of h in the s channel, where $\lambda_{H\phi}$ can be as small as 10^{-4}. The SM channel dominant samples via the Higgs portal distribute mainly on the upper edge of the allowed region of $\lambda_{H\phi}$. For the scalar semiannihilation dominant samples, $\lambda_{H\phi} \gtrsim 10^{-3}$ is required. The lower limit on $\lambda_{H\phi}$ for the $h\phi$ dominant channel grows as m_ϕ increases. So the contribution of the $\phi\phi \to h\phi$ channel is only important in the range of $[10^2, 10^3]$ GeV. Since the $h\phi$ channel also involves the cubic coupling μ, a not too small value of μ is required for

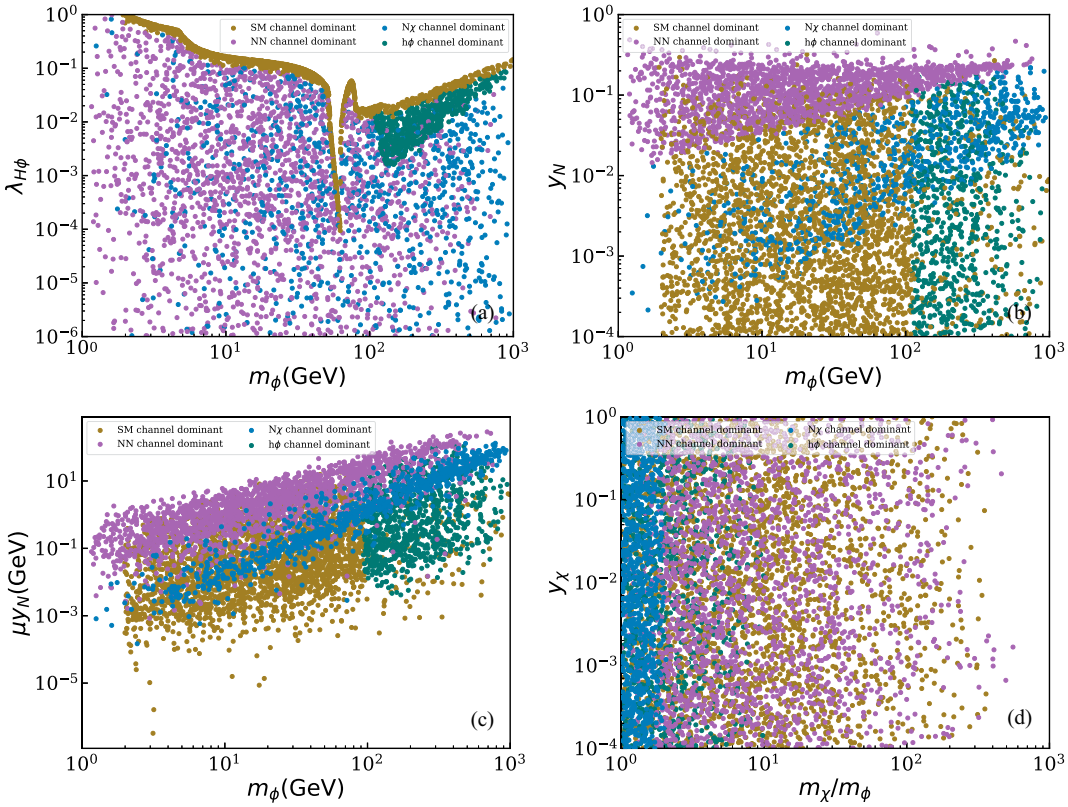

FIG. 6. Distributions of samples with correct relic density for scalar dark matter. The purple, blue, yellow, and green points denote that the dominant annihilation channel is $\phi\phi \to NN$, $\phi\phi \to N\chi$, $\phi\phi \to$ SM, and $\phi\phi \to h\phi$, respectively. Projection of allowed samples on (a) $\lambda_{h\phi} - m_\phi$ plane, (b) $y_N - m_\phi$ plane, (c) $\mu y_N - m_\phi$ plane, and (d) $y_\chi - m_\chi/m_\phi$ plane.

the $h\phi$ dominant samples. For the secluded channel $\phi\phi \to NN$ and the semiannihilation channel $\phi\phi \to N\chi$, lower limits on y_N are required as shown in Fig. 6(b), which is similar to the fermion dark matter. However, due to additional contributions from the $\phi\phi \to$ SM and $\phi\phi \to h\phi$ channels, y_N can be as small as 10^{-4} when m_ϕ is above $\mathcal{O}(10)$ GeV, which is different from the fermion dark matter. In Fig. 6(c), we show the corresponding parameters that are involved in the $\phi\phi \to N\chi$ channel. An approximate lower limit on the factor μy_N exists for $\phi\phi \to N\chi$ dominant samples. To make sure this semiannihilation channel is kinematically allowed, $m_\chi/m_\phi \lesssim (2m_\phi - m_N)/m_\phi \lesssim 2$ should be satisfied, which is depicted in Fig. 6(d). There is also a fake upper limit $m_\chi/m_\phi < 10$ for the $\phi\phi \to h\phi$ dominant samples, because it happens to be $m_\chi^{\max} \simeq 10^3$ and $m_\phi^{\min} \simeq 10^2$ GeV.

IV. HIGGS INVISIBLE DECAY

In principle, the light sterile neutrino could induce additional Higgs decay mode $h \to \nu N$ when $m_N \lesssim m_h$. However, with the seesaw predicted Yukawa coupling $y_\nu \sim \sqrt{2m_\nu m_N}/v \sim \mathcal{O}(10^{-6})$, the corresponding decay width is heavily suppressed. Meanwhile, for sufficient light dark matter, it can contribute to the Higgs invisible decay. The corresponding branching ratio has been constrained by the ATLAS experiment with [66]

$$\mathrm{Br}_{\mathrm{inv}} = \frac{\Gamma_{\mathrm{inv}}}{\Gamma_{\mathrm{inv}} + \Gamma_{\mathrm{SM}}} < 0.11, \tag{9}$$

where $\Gamma_{\mathrm{SM}} \simeq 4$ MeV is the standard Higgs width. The theoretical Higgs invisible decay widths into the dark matter are given by [45]

$$\Gamma(h \to \phi\phi) = \frac{\lambda_{H\phi}^2 v^2}{8\pi m_h}\sqrt{1 - \frac{4m_\phi^2}{m_h^2}}, \tag{10}$$

$$\Gamma(h \to \bar{\chi}\chi) = \frac{m_h (\lambda_{H\chi}^{\mathrm{eff}})^2}{8\pi}\left(1 - \frac{4m_\chi^2}{m_h^2}\right)^{3/2}, \tag{11}$$

where the one-loop effective $h\bar{\chi}\chi$ coupling is

$$\lambda_{H\chi}^{\mathrm{eff}} = \lambda_{H\phi}\frac{y_N^2}{16\pi^2}\frac{m_N}{(m_\phi^2 - m_N^2)^2}\left(m_\phi^2 - m_N^2 + m_N^2 \log\frac{m_N^2}{m_\phi^2}\right). \tag{12}$$

Figure 7 shows the theoretical branching ratios of Higgs invisible decay induced by dark matter and various constraints. For fermion dark matter in Fig. 7(a), the branching

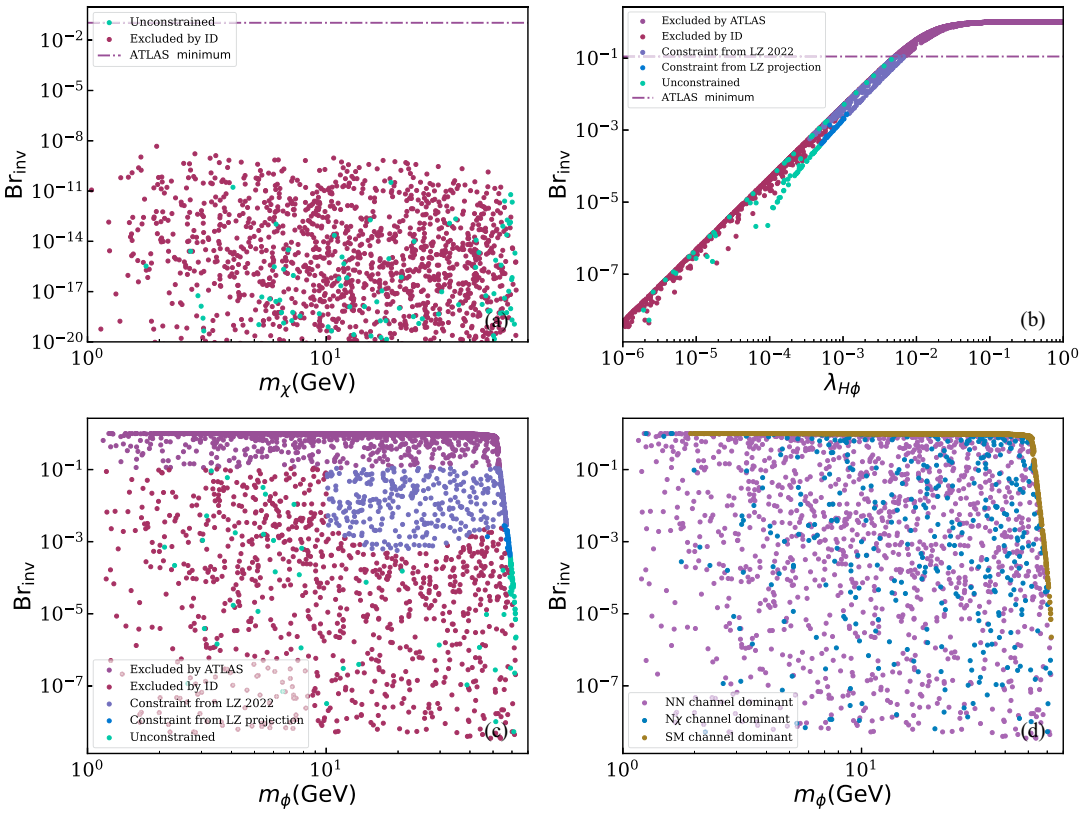

FIG. 7. Branching ratios of invisible Higgs decay induced by (a) fermion and (b)–(d) scalar dark matter. (a)–(c), the purple, slate blue, and red points are excluded by ATLAS search of Higgs invisible decay [66], direct detection of LZ [68], and indirect detection (ID) [33], respectively. The blue points satisfy all current constraints but are within the reach of the future LZ experiment [69], meanwhile the green points are unconstrained. In (d), we also classify the samples according to the dominant annihilation channels. Labels of the samples are the same as in Figs. 5 and 6.

ratio of Higgs invisible decay is below 10^{-9}, which is because of the loop suppression of effective Higgs coupling $\lambda_{H\chi}^{\mathrm{eff}}$. The predicted branching ratio is proportional to the coupling $\lambda_{H\phi}$. So even reaching the perturbation limit $\lambda_{H\phi} \sim 4\pi$, the Higgs invisible decay induced by fermion dark matter is less than 10^{-7}. Because the future high-luminosity LHC (HL-LHC) could only probe $\mathrm{Br_{inv}} \gtrsim 0.033$ [67], this negligible tiny branching ratio induced by fermion dark matter is thus far beyond the reach of direct collider measurement. As will be shown later, most samples in the light dark matter region below about 60 GeV are excluded by indirect searches.

The scenario for scalar dark matter is quite different, where $\mathrm{Br_{inv}}$ could be the dominant decay channel of Higgs when $\lambda_{H\phi} > 0.1$. Under current constraints, the region with $m_\phi \lesssim 53$ GeV and $\mathrm{Br_{inv}} > 0.11$ is excluded by the ATLAS experiment as shown in Figs. 7(b) and 7(c), which corresponds to $\lambda_{H\phi} \gtrsim 10^{-2}$ disallowed in this region. According to Fig. 7(d), most excluded samples in this region are dominantly annihilation via the $\phi\phi \to \mathrm{SM}$ channel. For $m_\phi \gtrsim 10$ GeV, the direct detection experiment LZ [68] sets a more stringent constraint than the Higgs invisible decay, where $\mathrm{Br_{inv}} \gtrsim 10^{-3}$ and $\lambda_{H\phi} \gtrsim 4 \times 10^{-4}$ might be excluded. Such a small branching ratio is also beyond the reach of the future HL-LHC [67]. For scalar dark matter lighter than 10 GeV, the Higgs invisible decay leads to more strict constraint than direct detection as shown in Fig. 7(c). The annihilation channels of samples in the region that escape the limits from Higgs invisible decay and direct detection are $\phi\phi \to NN$ and $\phi\phi \to N\chi$. Although this region is also tightly constrained by indirect detection, there are still some samples that satisfy all current constraints. We have checked that most of these light-mass survived samples annihilate via $\phi\phi \to N\chi$ with the special requirement $2m_\phi \lesssim m_N + m_\chi$. Therefore, if the HL-LHC discovers a relatively large $\mathrm{Br_{inv}}$, the dark matter candidate should be a scalar with mass around a few GeV, while the sterile neutrino is also at the GeV scale.

V. INDIRECT DETECTION

The indirect detection experiments aim to search for various types of particles produced in dark matter annihilation. The differential flux arising from the annihilation of dark matter is calculated as

$$\frac{d\Phi}{dE} = \frac{1}{4\pi}\frac{\langle\sigma v\rangle}{2m_{\rm DM}^2}\frac{dN}{dE}\cdot\int_{\Delta\Omega} d\Omega \int \rho_{\rm DM}^2(s)ds, \quad (13)$$

where $\rho_{\rm DM}$ is the dark matter density of the observed object. The energy spectrum dN/dE describes the distribution of observed particles from dark annihilation. According to previous studies, current indirect limits could constrain dark matter mass below about 50 GeV [34]. In this region, the dominant annihilation channels for both fermion and scalar dark matter are NN and $N\chi$ final states, after imposing the constraint from Higgs invisible decay. The resulting spectrum dN/dE depends on both the masses $m_{\rm DM}$ and m_N and decay modes of sterile neutrino N. With light $m_N < m_W$, the three-body decay width via off shell W and Z can be estimated as

$$\Gamma_N \approx \frac{G_f^2}{192\pi^3}|\theta_\alpha|^2 m_N^5, \quad (14)$$

where $\theta_\alpha(\alpha = e, \mu, \tau)$ describes the mixing angle between sterile and active neutrinos for different flavors. For a heavier

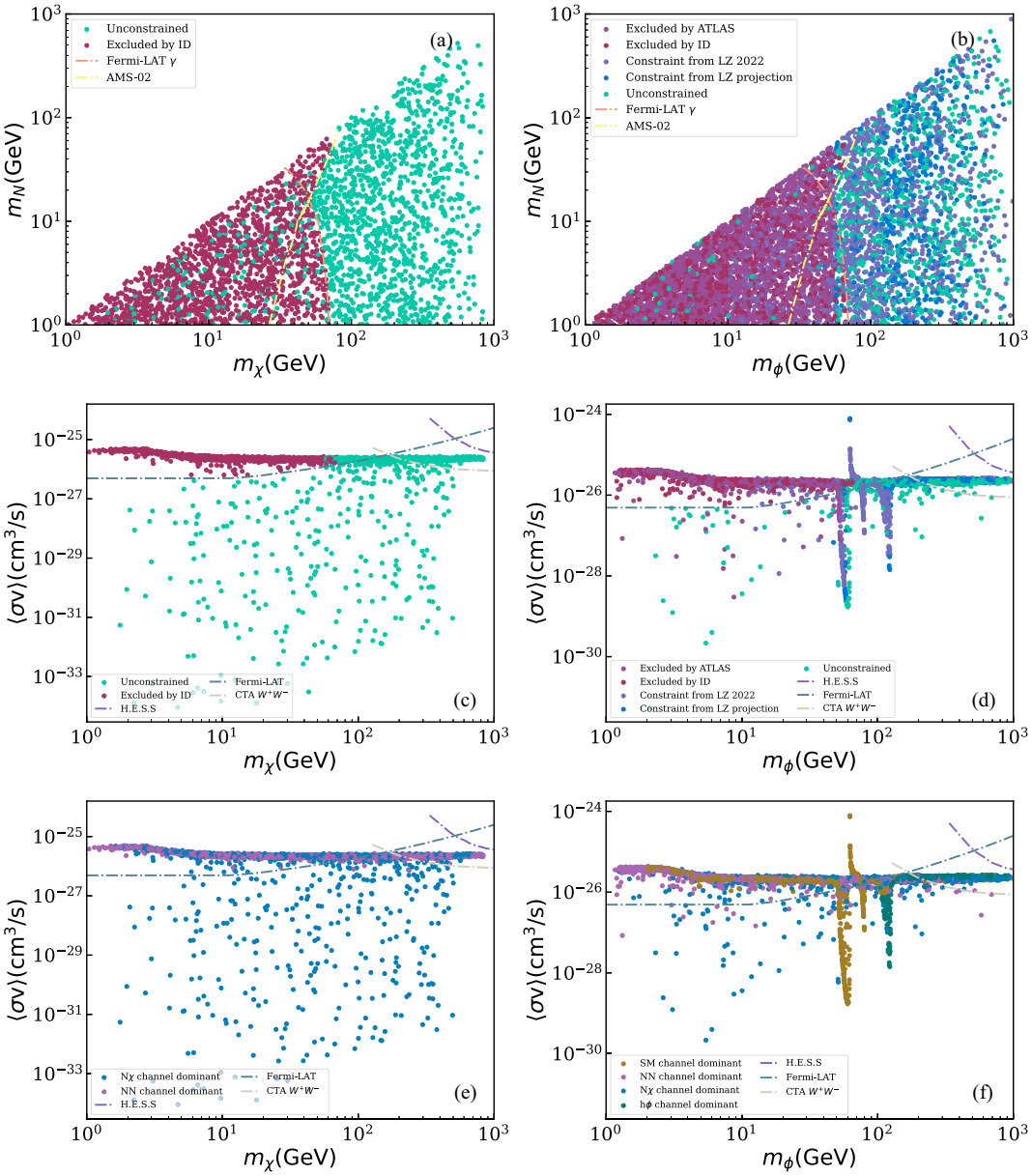

FIG. 8. Exclusion limits of indirect detection experiments. (a),(b) The yellow and orange curves represent the bounds of the antiproton-to-proton flux ratio from AMS-02 [70] and gamma rays in the Milky Way dwarf spheroidal galaxy from Fermi-LAT [71] with typical thermal annihilation cross section $\langle\sigma v\rangle = 2.2 \times 10^{-26}$ cm^3 s^{-1}. (c)–(f) The blue and purple curves illustrate the limits on the annihilation cross section from Fermi-LAT and H.E.S.S. [33]. The yellow line shows the sensitivity of future CTA experiment for the W^+W^- annihilation modes [72]. Other labels are the same as in Fig. 7.

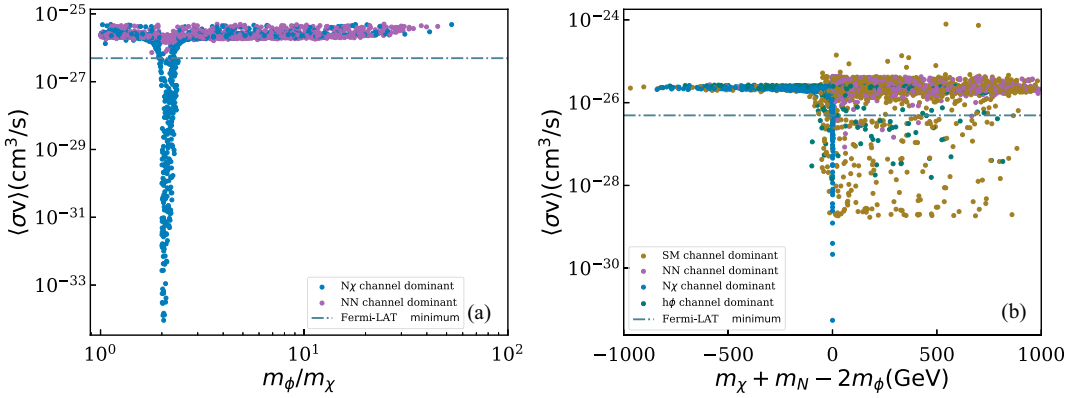

FIG. 9. Annihilation cross section for indirect detection. The horizontal dash-dotted line is the minimum value of the Fermi-LAT limit in Fig. 8. (a) Annihilation cross section as function of m_ϕ/m_χ for fermion dark matter. (b) Annihilation cross section as function of $m_\chi + m_N - 2m_\phi$ for scalar dark matter.

sterile neutrino, the two-body decays $N \to W^\pm \ell^\mp, Z\nu, h\nu$ are the dominant channels. The continuum spectra of muon flavor N is similar to the electron flavor scenario, while the tau flavor N produces a slightly stronger gamma-ray spectrum [33]. In this paper, we consider an electron flavor N for a conservative study.

Using the observed spectra, the exclusion limits on dark matter annihilation can be derived by performing a likelihood analysis, although the large astrophysical uncertainties can affect these limits. In Fig. 8, we show the indirect detection constraints from the antiproton observations of AMS-02 and the gamma-ray observations of Fermi-LAT [34]. For light $m_N \sim \mathcal{O}$ (GeV), the Fermi-LAT experiment could rule out $m_{\mathrm{DM}} \lesssim 60$ GeV. Meanwhile, for heavier m_N, the AMS-02 result would exclude $m_{\mathrm{DM}} \lesssim 80$ GeV. The combination of these two limits excludes most samples in the region below $m_{\mathrm{DM}} \lesssim 50$ GeV. It is notable that these two limits in Figs. 8(a) and 8(b) are obtained with fixed thermal annihilation cross section $\langle\sigma v\rangle = 2.2 \times 10^{-26}$ cm^3 s^{-1}. In Figs. 8(c)–8(f), we show the theoretically predicted annihilation cross section for indirect detection, where the cross sections of the semi-annihilation process as $\chi\chi/\phi\phi \to N\chi$, $\phi\phi \to h\phi$ are multiplied by a factor of $1/2$. Since the annihilation cross section today can be much smaller than the thermal target $\langle\sigma v\rangle = 2.2 \times 10^{-26}$ cm^3 s^{-1}, we require that the samples are excluded by indirect detection when the corresponding cross sections are also above the Fermi-LAT limit on $\langle\sigma v\rangle$.

In the low mass region below 50 GeV, the two annihilation channels of fermion dark matter lead to quite different results, as shown in Fig. 9(a). For the $\chi\chi \to NN$ dominant samples, the corresponding annihilation cross sections are at the typical value $\langle\sigma v\rangle = 2.2 \times 10^{-26}$ cm^3 s^{-1}, so these samples are excluded by indirect detection. However for the $\chi\chi \to N\chi$ dominant samples, due to the existence of the s-channel contribution via the dark scalar ϕ, the annihilation cross section could be much smaller than 2.2×10^{-26} cm^3 s^{-1} when $2m_\chi \simeq m_\phi$. In this special scenario, the $\chi\chi \to N\chi$ dominant samples also satisfy the indirect constraints. For the scalar dark matter, although there are three annihilation modes in these low mass regions, the $\phi\phi \to$ SM channel is tightly constrained by Higgs invisible decay and direct detection.

Similar to the fermion dark matter, most of the $\phi\phi \to NN$ dominant samples could be excluded by indirect detection in the low mass region, while some of the $\phi\phi \to N\chi$ dominant samples are still allowed. Although there is no on shell s-channel contribution of the $\phi\phi \to N\chi$ channel, we find that the allowed samples satisfy $2m_\phi \lesssim m_\chi + m_N$ as shown in Fig. 9(b). So these samples fall into the forbidden region, where the nonrelativistic velocity of dark matter today cannot overcome the mass splitting $m_\chi + m_N - 2m_\phi$ [73]. The scalar dark matter annihilation into SM particles also has on shell s-channel contributions when $2m_\phi \simeq m_h$. Meanwhile, the scalar semiannihilation $\phi\phi \to h\phi$ meets the forbidden condition when $m_\phi \lesssim m_h$. The resulting annihilation cross sections of these two kinds are much smaller than the typical value $\langle\sigma v\rangle = 2.2 \times 10^{-26}$ cm^3 s^{-1}, so these samples are hard to probe by indirect detection.

For dark matter around the TeV scale, the most stringent constraint is from H.E.S.S. observation [74], which is shown in Figs. 8(c) and 8(d). At present, no samples could be excluded by H.E.S.S. If there is no positive signal at future direct detection experiments, the scalar semiannihilation $\phi\phi \to h\phi$ would be excluded. So in this heavy mass region, we only consider the sterile neutrino portal annihilation channels $\phi\phi/\chi\chi \to NN$. Because the photon spectrum from the NN final state is similar to the W^+W^- final state, we also show the future limits from the Cherenkov Telescope Array (CTA) [72], which will cover most samples above 200 GeV.

VI. DIRECT DETECTION

In this model, the dark matter scatters off the atomic nucleus elastically via the t-channel exchange of the Higgs boson h. For scalar dark matter, this scattering happens at

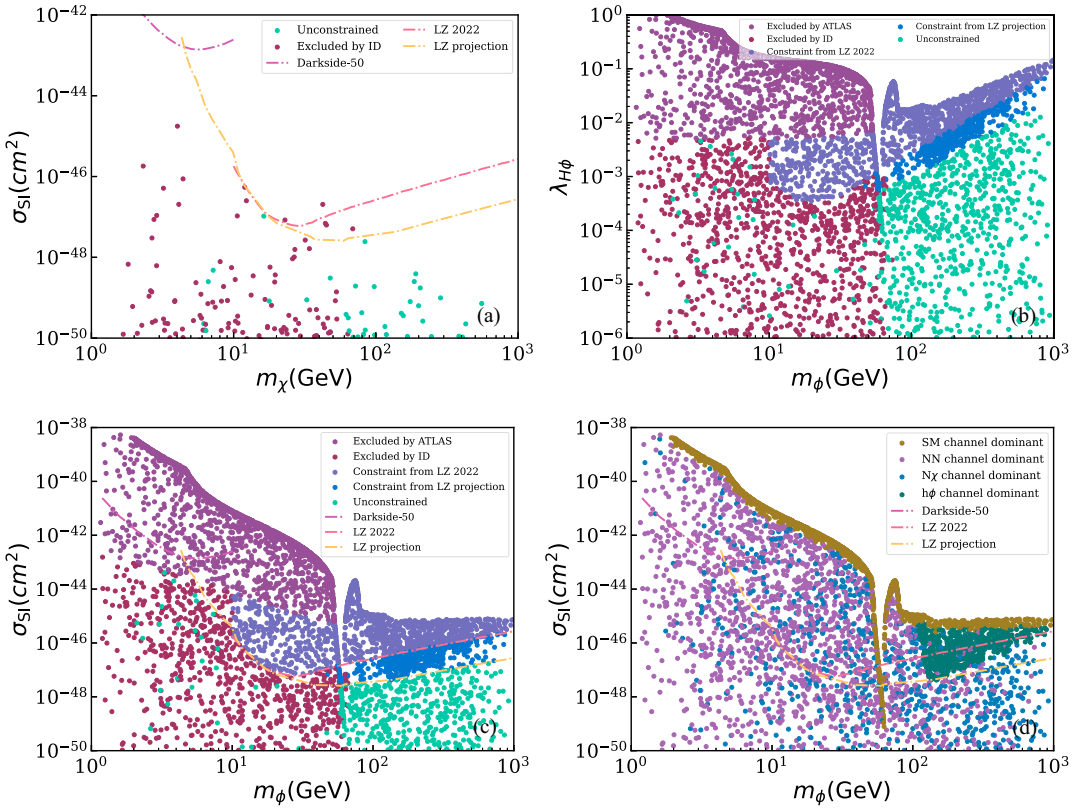

FIG. 10. The predicted spin-independent cross section and various exclusion limits. The purple and red lines are the current exclusion limits from DarkSide-50 and LZ, respectively. The yellow line is the projected LZ limit. Other labels are the same as in Fig. 7. (a) is for fermion dark matter and (b)–(d) are for scalar dark matter.

tree level, while for fermion dark matter, it is induced at one-loop level [45]. The dark matter direct detection experiments measure the nuclear recoil energy and place constraints on the dark matter–nucleon scattering cross section. Until now, no concrete signal is observed by direct detection experiments, such as PandaX-4T [75], XENONnT [76], and LZ [68]. In this paper, we consider the most stringent limit from LZ and DarkSide-50 [77] at present and the future projected limit from LZ [69]. For light dark matter below about 10 GeV, the DarkSide-50 experiment sets the most stringent limit, which excludes $\sigma_{\rm SI} \gtrsim 10^{-43}$ cm^2. For heavier dark matter, the LZ limit is the most tight one, where the minimum is at $m_{\rm DM} = 30$ GeV with $\sigma_{\rm SI} = 5.9 \times 10^{-48}$ cm^2.

Within the context of the Higgs portal effective scenarios [78], the spin-independent (SI) cross section for dark matter collision with the nucleon can be expressed as

$$\sigma_{\rm SI}^{\phi n} = \frac{\lambda_{H\phi}^2}{\pi m_h^4} \frac{m_n^4 f_n^2}{(m_\phi + m_n)^2}, \tag{15}$$

$$\sigma_{\rm SI}^{\chi n} = \frac{(\lambda_{H\chi}^{\rm eff})^2}{\pi m_h^4} \frac{m_n^4 m_\chi^2 f_n^2}{(m_\chi + m_n)^2}. \tag{16}$$

The nucleon mass is denoted as m_n, and the parameter $f_n \simeq 0.3$ is used to parametrize the Higgs-nucleon interactions [4]. The effective coupling $\lambda_{H\chi}^{\rm eff}$ is calculated in Eq. (12).

The scan results are shown in Fig. 10 for both fermion and scalar dark matter. Because the scattering cross section for fermion dark matter is suppressed by the one-loop factor, the predicted values are typically well below the current experimental limits. Within the parameter space scanned in Eq. (8), even the future projection of the LZ experiment could not have a positive signature when taking into account the limits from indirect detection as shown in Fig. 10(a). We also find that samples with relatively large scattering cross section $\sigma_{\rm SI} \gtrsim 10^{-50}$ cm^2 are dominant by the semiannihilation channel $\chi\chi \to N\chi$. In principle, increasing the maximum values of related coupling $\lambda_{H\phi}$ and y_N to the perturbation limits could lead to the predicted scattering cross section above current limits [45]. These detectable samples are expected to annihilate via the $\chi\chi \to N\chi$ channel in this model.

As for the scalar dark matter, the coupling $\lambda_{H\phi}$ induces quite a large scattering cross section with correct relic density. The direct detection experiments, such as LZ, could now exclude samples with $\lambda_{H\phi} \gtrsim 4 \times 10^{-4}$. As already discussed in Sec. IV, the Higgs invisible decay has excluded $\lambda_{H\phi} \gtrsim 10^{-2}$ for $m_\phi < m_h/2$. It is clear in Fig. 10(c) that the exclusion limit from Higgs invisible decay is more stringent than the direct limit from DarkSide-50; therefore, we do not consider the DarkSide-50 limit in

this study. For $m_\phi \gtrsim 10$ GeV, the direct limit from LZ is over 2 orders of magnitudes tighter than the Higgs invisible limit. Since the indirect detection has already excluded most samples with $m_\phi \lesssim 50$ GeV, the future projection of LZ is also hard to probe the allowed samples in this region. Together with Fig. 10(d), the only viable region of $\phi\phi \to$ SM dominant samples is the narrow resonance region at $m_\phi \lesssim m_h/2$. The predicted cross section of SM dominant samples can be as small as $\sigma_{\rm SI} \sim 10^{-49}$ cm^2, which is also beyond the reach of the future LZ.

For heavier scalar dark matter above 100 GeV, only the direct detection experiments now set the corresponding limits. The $\phi\phi \to$ SM dominant samples lead to the largest predicted cross section $\sigma_{\rm SI} \simeq 10^{-45}$ cm^2, which is disfavored by the current LZ limit when $m_\phi < 1$ TeV. It is still possible for $\phi\phi \to$ SM dominant samples with m_ϕ above 1 TeV [79], but it is out of the parameter space we scanned in Eq. (8). The new contribution of the semiannihilation $\phi\phi \to h\phi$ channel would induce a smaller scattering cross section. Since this semiannihilation channel also involves the cubic coupling, the stability and unitarity bounds $\mu < 3m_\phi$ then lead to a lower bound for the predicted cross section, as shown in Fig. 10(d). For instance, the minimum predicted cross section is about 3×10^{-47} cm^2 with $m_\phi \sim 130$ GeV. Once $\phi\phi \to h\phi$ is kinematically allowed, this lower bound on $\sigma_{\rm SI}$ increases as m_ϕ is larger. Under the current LZ limit, some of the $\phi\phi \to h\phi$ dominant samples are still allowed. In the future, the projected LZ limit could probe all the $\phi\phi \to h\phi$ dominant samples. So if there is still no positive signature at the future LZ, the allowed samples will be dominant by $\phi\phi \to NN$ and $\phi\phi \to N\chi$ channels. We then expect observable signatures at indirect detection experiments from these two channels for most of the allowed parameter space.

VII. CONCLUSION AND DISCUSSION

In addition to generating tiny neutrino mass via the type-I seesaw mechanism, the electroweak scale sterile neutrino N can also mediate the interaction between the dark sector and the standard model. Beyond the simplest Z_2 symmetry, we extend the sterile neutrino portal dark matter with Z_3 symmetry in this paper. We introduce a scalar singlet ϕ and a fermion singlet χ to the dark sector. Under the dark Z_3 symmetry, the dark sector transforms as $\chi \to e^{i2\pi/3}\chi$, $\phi \to e^{i2\pi/3}\phi$, while the standard model particles and the sterile neutrinos transform trivially. In this paper, we consider WIMP dark matter for both scalar and fermion scenarios. The Z_3 symmetry introduces two new interactions, i.e., $y_\chi \phi \overline{\chi^c}\chi$ and $\mu\phi^3/2$, which lead to semiannihilation channels as $\chi\chi \to N\chi$ and $\phi\phi \to h\phi$.

For the fermion dark matter χ, the annihilation channels are secluded $\chi\chi \to NN$ and the semiannihilation $\chi\chi \to N\chi$. Because the effective $h\overline{\chi}\chi$ coupling is induced at the one-loop level, the contribution of fermion dark matter to Higgs invisible decay is negligibly tiny. The resulting dark matter–nucleon scattering cross section is also beyond the reach of future experiments. Currently, the indirect detection could exclude most of the samples with $m_\chi \lesssim 50$ GeV. In the future, the CTA experiment is expected to probe the high mass region. However, due to the s-channel contribution of dark scalar ϕ to the semiannihilation $\chi\chi \to N\chi$, the corresponding annihilation cross section is much smaller than the usual thermal value $\langle\sigma v\rangle = 2 \times 10^{-26}$ cm^3 s^{-1} when $2m_\chi \simeq m_\phi$. In this special scenario, even the indirect detection cannot have a positive signature.

For the scalar dark matter ϕ, there are four kinds of annihilation channels, i.e., the Higgs portal $\phi\phi \to$ SM, the secluded channel $\phi\phi \to NN$, and the semiannihilations $\phi\phi \to N\chi, h\phi$. The direct Higgs portal interaction $\lambda_{H\phi}(H^\dagger H)(\phi^\dagger\phi)$ generates observable signatures from Higgs invisible decay and indirect and direct detection. Under these constraints, the Higgs portal $\phi\phi \to$ SM dominant samples are only viable at the resonance region $m_\phi \lesssim m_h/2$ for the dark scalar below 1 TeV. The semiannihilation $\phi\phi \to h\phi$ might be the dominant one in the range of $[10^2, 10^3]$ GeV. This channel predicts a lower bound on the dark matter–nucleon scattering cross section, which can be fully detected by the future LZ experiment. Meanwhile, the secluded $\phi\phi \to NN$ and semiannihilation $\phi\phi \to N\chi$ channels can easily satisfy current bounds and are promising at indirect detection experiments. Although the light-mass region is tightly constrained, we find that, when the forbidden relation $2m_\phi \lesssim m_\chi + m_N$ is satisfied, the semiannihilation channel $\phi\phi \to N\chi$ also has a suppressed annihilation cross section for indirect detection.

Compared to the Z_2 symmetric model, the new interactions introduced in the Z_3 symmetric model enlarge the viable parameter space. In Table I, we summarize the different signatures for the Z_2 and Z_3 symmetric models. For instance, light dark matter below about 50 GeV is completely excluded by indirect detection in the Z_2 symmetric model.[1] However, in the Z_3 symmetric model, the semiannihilation $\chi\chi \to N\chi$ and $\phi\phi \to N\chi$ are still allowed under certain circumstances. Therefore, once light dark matter is discovered in future indirect detection experiments, the Z_3 symmetric model will be preferred. If such light dark matter candidate is the scalar ϕ, then testable Higgs invisible decay is also expected. In the future, all dark matter scenarios with mass above 200 GeV could lead to observable signature at CTA. The energy spectrum dN/dE from pair annihilation $\chi\chi \to NN$ is different from semiannihilation $\chi\chi \to \chi N$, which might be distinguished by likelihood analysis, in principle. For scalar dark matter ϕ, there is further positive direct

[1]If the neutrinos are Dirac particles, the dark matter annihilation cross sections are p-wave suppressed today [29]; therefore, light dark matter is still allowed in the Z_2 symmetry.

TABLE I. Different signatures for the Z_2 and Z_3 symmetric model.

Dark matter	Symmetry	$h \to \text{inv}$	$m_{\text{DM}} \lesssim 50$ GeV	Future CTA	Beyond CTA	Direct detection
χ	Z_2	✗	✗	✓	✗	✗
	Z_3	✗	✓	✓	✓	✗
ϕ	Z_2	✗	✗	✓	✗	✓
	Z_3	✓	✓	✓	✗	✓

detection signals. However, if no concrete signature is observed by future CTA, then only the fermion dark matter χ under the Z_3 symmetry is allowed for heavy dark matter.

Finally, let us consider the dark sector under the Z_4 symmetry, which transforms as $\phi \to -\phi$ and $\chi \to i\chi$ [80–82]. One promising scenario is $m_\phi < 2m_\chi$, which leads to both χ and ϕ stable, i.e., two-component dark matter scenario. In contrast, the next-to-lightest particle in the Z_3 model is unstable. For example, the dark scalar can decay via $\phi \to \chi N$ or $\phi \to \chi\nu$ when χ is the dark matter. Under the Z_4 symmetry, the sterile neutrino portal coupling $y_N\phi\bar{\chi}N$ and the cubic term $\mu\phi^3/2$ are forbidden. Therefore, the secluded channels $\chi\chi \to NN$ and $\phi\phi \to NN$ and semiannihilation channels $\chi\chi \to \chi N$, $\phi\phi \to \chi N$, and $\phi\phi \to h\phi$ will not appear. The Higgs portal coupling $\lambda_{H\phi}(H^\dagger H)(\phi^\dagger\phi)$ and dark Yukawa coupling $(y_s\overline{\chi^c}\chi + y_p\overline{\chi^c}\gamma_5\chi)\phi$ are still allowed by the Z_4 symmetry. The typical annihilation channels in the Z_4 model are $\chi\chi \to \phi h$ and $\phi\chi \to \chi h$ [80], which is clearly different from the Z_3 symmetry. Most samples with correct relic density in the Z_4 symmetry can be probed by direct detection, but are beyond the reach of the future CTA [80]. More sophisticated symmetries can be found in Ref. [83].

ACKNOWLEDGMENTS

This work is supported by the National Natural Science Foundation of China under Grants No. 11805081 and 11635009, Natural Science Foundation of Shandong Province under Grants No. ZR2019QA021 and No. ZR2022MA056, and the Open Project of Guangxi Key Laboratory of Nuclear Physics and Nuclear Technology under Grant No. NLK2021-07.

[1] G. Arcadi, M. Dutra, P. Ghosh, M. Lindner, Y. Mambrini, M. Pierre, S. Profumo, and F. S. Queiroz, Eur. Phys. J. C **78**, 203 (2018).
[2] C. P. Burgess, M. Pospelov, and T. ter Veldhuis, Nucl. Phys. **B619**, 709 (2001).
[3] J. McDonald, Phys. Rev. D **50**, 3637 (1994).
[4] J. M. Cline, K. Kainulainen, P. Scott, and C. Weniger, Phys. Rev. D **88**, 055025 (2013); **92**, 039906(E) (2015).
[5] A. Alves, S. Profumo, and F. S. Queiroz, J. High Energy Phys. 04 (2014) 063.
[6] A. Alves, A. Berlin, S. Profumo, and F. S. Queiroz, Phys. Rev. D **92**, 083004 (2015).
[7] W. Rodejohann and C. E. Yaguna, J. Cosmol. Astropart. Phys. 12 (2015) 032.
[8] M. Klasen, F. Lyonnet, and F. S. Queiroz, Eur. Phys. J. C **77**, 348 (2017).
[9] P. Minkowski, Phys. Lett. **67B**, 421 (1977).
[10] R. N. Mohapatra and G. Senjanovic, Phys. Rev. Lett. **44**, 912 (1980).
[11] S. Dodelson and L. M. Widrow, Phys. Rev. Lett. **72**, 17 (1994).
[12] A. Boyarsky, M. Drewes, T. Lasserre, S. Mertens, and O. Ruchayskiy, Prog. Part. Nucl. Phys. **104**, 1 (2019).
[13] B. M. Roach, K. C. Y. Ng, K. Perez, J. F. Beacom, S. Horiuchi, R. Krivonos, and D. R. Wik, Phys. Rev. D **101**, 103011 (2020).
[14] A. Boyarsky, J. Franse, D. Iakubovskyi, and O. Ruchayskiy, Phys. Rev. Lett. **115**, 161301 (2015).
[15] B. M. Roach, S. Rossland, K. C. Y. Ng, K. Perez, J. F. Beacom, B. W. Grefenstette, S. Horiuchi, R. Krivonos, and D. R. Wik, Phys. Rev. D **107**, 023009 (2023).
[16] E. Ma, Phys. Rev. D **73**, 077301 (2006).
[17] E. Ma, Phys. Lett. B **662**, 49 (2008).
[18] R. Ding, Z. L. Han, Y. Liao, and W. P. Xie, J. High Energy Phys. 05 (2016) 030.
[19] J. Liu, Z. L. Han, Y. Jin, and H. Li, J. High Energy Phys. 12 (2022) 057.
[20] A. Falkowski, J. Juknevich, and J. Shelton, arXiv:0908.1790.
[21] A. Falkowski, J. T. Ruderman, and T. Volansky, J. High Energy Phys. 05 (2011) 106.
[22] V. Gonzalez Macias and J. Wudka, J. High Energy Phys. 07 (2015) 161.
[23] V. González-Macías, J. I. Illana, and J. Wudka, J. High Energy Phys. 05 (2016) 171.
[24] M. Blennow, E. Fernandez-Martinez, A. Olivares-Del Campo, S. Pascoli, S. Rosauro-Alcaraz, and A. V. Titov, Eur. Phys. J. C **79**, 555 (2019).

[25] P. Ballett, M. Hostert, and S. Pascoli, Phys. Rev. D **101**, 115025 (2020).
[26] E. Hall, T. Konstandin, R. McGehee, and H. Murayama, Phys. Rev. D **107**, 055011 (2023).
[27] A. Liu, Z. L. Han, Y. Jin, and F. X. Yang, Phys. Rev. D **101**, 095005 (2020).
[28] E. Hall, R. McGehee, H. Murayama, and B. Suter, Phys. Rev. D **106**, 075008 (2022).
[29] L. Coito, C. Faubel, J. Herrero-García, A. Santamaria, and A. Titov, J. High Energy Phys. 08 (2022) 085.
[30] A. Liu, F. L. Shao, Z. L. Han, Y. Jin, and H. Li, Eur. Phys. J. C **83**, 423 (2023).
[31] M. Pospelov, A. Ritz, and M. B. Voloshin, Phys. Lett. B **662**, 53 (2008).
[32] Y. L. Tang and S. h. Zhu, J. High Energy Phys. 03 (2016) 043.
[33] M. D. Campos, F. S. Queiroz, C. E. Yaguna, and C. Weniger, J. Cosmol. Astropart. Phys. 07 (2017) 016.
[34] B. Batell, T. Han, and B. Shams Es Haghi, Phys. Rev. D **97**, 095020 (2018).
[35] B. Batell, T. Han, D. McKeen, and B. Shams Es Haghi, Phys. Rev. D **97**, 075016 (2018).
[36] M. G. Folgado, G. A. Gómez-Vargas, N. Rius, and R. Ruiz De Austri, J. Cosmol. Astropart. Phys. 08 (2018) 002.
[37] A. Falkowski, E. Kuflik, N. Levi, and T. Volansky, Phys. Rev. D **99**, 015022 (2019).
[38] M. Becker, Eur. Phys. J. C **79**, 611 (2019).
[39] M. Chianese and S. F. King, J. Cosmol. Astropart. Phys. 09 (2018) 027.
[40] P. Bandyopadhyay, E. J. Chun, and R. Mandal, J. Cosmol. Astropart. Phys. 08 (2020) 019.
[41] Y. Cheng and W. Liao, Phys. Lett. B **815**, 136118 (2021).
[42] Z. F. Chang, Z. X. Chen, J. S. Xu, and Z. L. Han, J. Cosmol. Astropart. Phys. 06 (2021) 006.
[43] B. Barman, P. S. Bhupal Dev, and A. Ghoshal, Phys. Rev. D **108**, 035037 (2023).
[44] A. Liu, F. L. Shao, Z. L. Han, Y. Jin, and H. Li, arXiv: 2212.10043.
[45] M. Escudero, N. Rius, and V. Sanz, Eur. Phys. J. C **77**, 397 (2017).
[46] M. Escudero, N. Rius, and V. Sanz, J. High Energy Phys. 02 (2017) 045.
[47] B. Batell, Phys. Rev. D **83**, 035006 (2011).
[48] M. Hirsch, S. Morisi, E. Peinado, and J. W. F. Valle, Phys. Rev. D **82**, 116003 (2010).
[49] J. L. Diaz-Cruz and E. Ma, Phys. Lett. B **695**, 264 (2011).
[50] G. Belanger, K. Kannike, A. Pukhov, and M. Raidal, J. Cosmol. Astropart. Phys. 04 (2012) 010.
[51] G. Belanger, K. Kannike, A. Pukhov, and M. Raidal, J. Cosmol. Astropart. Phys. 01 (2013) 022.
[52] A. Ghosh, D. Ghosh, and S. Mukhopadhyay, J. High Energy Phys. 08 (2020) 149.
[53] P. Bandyopadhyay, D. Choudhury, and D. Sachdeva, Phys. Rev. D **107**, 015020 (2023).
[54] D. K. Ghosh, P. Ghosh, and S. Jeesun, J. Cosmol. Astropart. Phys. 07 (2023) 012.
[55] A. Liu, F. L. Shao, Z. L. Han, Y. Jin, and H. Li, arXiv: 2308.12588.
[56] A. M. Abdullahi, P. B. Alzas, B. Batell, J. Beacham, A. Boyarsky, S. Carbajal, A. Chatterjee, J. I. Crespo-Anadon, F. F. Deppisch, A. De Roeck *et al.*, J. Phys. G **50**, 020501 (2023).
[57] A. Hektor, A. Hryczuk, and K. Kannike, J. High Energy Phys. 03 (2019) 204.
[58] F. D'Eramo and J. Thaler, J. High Energy Phys. 06 (2010) 109.
[59] Y. Cai and A. P. Spray, J. High Energy Phys. 01 (2016) 087.
[60] J. Guo, Z. Kang, and P. Zhang, Phys. Lett. B **826**, 136885 (2022).
[61] S. P. Li and X. J. Xu, J. Cosmol. Astropart. Phys. 06 (2023) 047.
[62] G. Bélanger, F. Boudjema, A. Goudelis, A. Pukhov, and B. Zaldivar, Comput. Phys. Commun. **231**, 173 (2018).
[63] T. Binder, T. Bringmann, M. Gustafsson, and A. Hryczuk, Phys. Rev. D **96**, 115010 (2017); **101**, 099901(E) (2020).
[64] N. Aghanim *et al.* (Planck Collaboration), Astron. Astrophys. **641**, A6 (2020); **652**, C4(E) (2021).
[65] O. Ruchayskiy and A. Ivashko, J. Cosmol. Astropart. Phys. 10 (2012) 014.
[66] ATLAS Collaboration, Combination of searches for invisible Higgs boson decays with the ATLAS experiment, Report No. ATLAS-CONF-2020-052.
[67] ATLAS Collaboration, Projections for measurements of Higgs boson cross sections, branching ratios, coupling parameters and mass with the ATLAS detector at the HL-LHC, Report No. ATL-PHYS-PUB-2018-054.
[68] J. Aalbers *et al.* (LZ Collaboration), Phys. Rev. Lett. **131**, 041002 (2023).
[69] D. S. Akerib *et al.* (LZ Collaboration), arXiv:1509.02910.
[70] M. Aguilar *et al.* (AMS Collaboration), Phys. Rev. Lett. **117**, 091103 (2016).
[71] M. Ackermann *et al.* (Fermi-LAT Collaboration), Phys. Rev. Lett. **115**, 231301 (2015).
[72] J. Carr *et al.* (CTA Collaboration), Proc. Sci. ICRC2015 (**2016**) 1203 [arXiv:1508.06128].
[73] R. T. D'Agnolo and J. T. Ruderman, Phys. Rev. Lett. **115**, 061301 (2015).
[74] A. Abramowski *et al.* (H.E.S.S. Collaboration), Phys. Rev. Lett. **106**, 161301 (2011).
[75] Y. Meng *et al.* (PandaX-4T Collaboration), Phys. Rev. Lett. **127**, 261802 (2021).
[76] E. Aprile *et al.* (XENON Collaboration), Phys. Rev. Lett. **131**, 041003 (2023).
[77] P. Agnes *et al.* (DarkSide-50 Collaboration), Phys. Rev. D **107**, 063001 (2023).
[78] G. Arcadi, A. Djouadi, and M. Kado, Eur. Phys. J. C **81**, 653 (2021).
[79] P. Athron, J. M. Cornell, F. Kahlhoefer, J. Mckay, P. Scott, and S. Wild, Eur. Phys. J. C **78**, 830 (2018).
[80] C. E. Yaguna and Ó. Zapata, Phys. Rev. D **105**, 095026 (2022).
[81] C. E. Yaguna and Ó. Zapata, arXiv:2308.05249.
[82] A. Bas i Beneito, J. Herrero-García, and D. Vatsyayan, J. High Energy Phys. 10 (2022) 075.
[83] C. E. Yaguna and Ó. Zapata, J. High Energy Phys. 03 (2020) 109.